Egyptian Journal of Chemistry

http://ejchem.journals.ekb.eg/

Optical and Electrochemical Investigations of CdSe (NPs) Based on Nonionic Surfactant for Carbon Steel Corrosion Control in 1 M HCl Solution

Mohamed Deef Allah*[1], S.S. Fouad[2], Samar Abdelhamed[1,3], A. Elaraby[4], M. Nabil[1,3].
[1]*Department of Basic Engineering Sciences, Faculty of Engineering (Shoubra), Benha University, Benha, Egypt.*
[2]*Department of Physics, Faculty of Education, Ain Shams University, Cairo 11566, Egypt*
[3]*Faculty of Engineering, Benha National University, Obour Campus, Egypt*
[4]*Egyptian Petroleum Research Institute, Nasr City 11727, Cairo, Egypt*

Abstract

In the present study, CdSe Nanoparticles (*CdSe-NPs*) were characterized using UV-vis (ultraviolet) and TEM (transmission electron microscope) and added to nonionic surfactant (*NS*) with different ratios (1, 2, 3 and 4 wt%) of to formulate *CdSe-NS* nanocomposite for caron steel (*CS*) corrosion control. The inhibition effect of the prepared inhibitor was investigated via electrochemical techniques such as electrochemical impedance spectroscopy (EIS) and potentiodynaminc polarization (PDP) besides weight loss measurements. The data obtained from EIS showed that, the addition of *CdSe-NPs* enhanced the inhibition efficacy of the prepared inhibitor till reach 96.55% at *4%wt-CdSe-NS* compared with that value at *0%wt-CdSe-NS* was 91.59% which indicated the role of *CdSe-NPs* in *CS* protection. While, PDP showed that the prepared inhibitors acted as mixed-type inhibitors. The corresponding dielectric functions (DF) are discussed in the light of the optoelectrical parameters and dispersion parameters. The strong sorption ability of *CdSe-NS*, resulting in the creation of a monolayer, which isolate *CS* surface from the corrosive environment and hence reduces its attack through the absorption process as well. Also, Atomic Force Microscope (AFM) was applied for more information about *CS* surface morphology.

Keywords: *Carbon steel, Corrosion inhibitors, Nanoparticles, Nonionic surfactant, Electrochemical measurements*

Introduction

Chemical corrosion inhibitors are widely used in manufacturing and processing operations. Nevertheless, the challenge is, when added to a corrosion system, to protect the material by decreasing the corrosion rate of the material that meets the fluid, which is typically a metal or alloy [1,2]. The corrosion detection problem nowadays is crucial to the accurate estimation of corrosion level under various conditions [3]. Understanding surfactant actions in a corrosion environment is critical for optimal surfactant use as corrosion inhibitor. Surfactant is environmentally acceptable and is very economical and easily available. Due to these characteristics, various potential applications such as corrosion inhibitor, detergent and petroleum oil recovery had been invented [5, 6]. In addition, surfactant as a corrosion inhibitor play an essential supporting role in catalysis, as well as nanotechnology science [7, 8]. The inhibition efficiency is determined by the inhibitor's chemical structure furthermore to the hydrophobic groups of surface-active agents. The functional of hydroxyl groups such as the propylene oxide, carbonyl, double bond, benzene ring, oxygen atom, and semiconductor atoms are responsible for improving their absorption ability on the surface of the steel [9, 10]. *CS* is an important component in the construction field; thus, the scientists focused their research on developing effective inhibition efficiencies of it [10]. Surfactants have the potential to play a role, in nanotechnology science as corrosion inhibitors, to protect steel from corrosion [11–13].

The mitigation mechanism of corrosion inhibitors (CIs) can be clarified by a protective layer construction over shielding *CS* surface through the adsorption process based on CIs chemical structure. Shengjie Du et al. [14] studied the mitigation performance of HPAE-Ohs for Q235-steel in 1 M HCl solution using various chemical and electrochemical methods showing that, HPAE-OHs acted as a mixed type inhibitor with 94.9% efficiency. Wenjing Liu et al. [15] evaluated the prepared UPy-D400-PEGDA as corrosion inhibitor for *CS* in 1 M HCl. UPy-D400-PEGDA mitigation potency increased till reaching 98.80% at 500 mg/L. N. Punitha et al. [16] presented the effect of PCBPE on mild steel in 1 M HCl solution at different temperatures. The results obtained exhibited that the prepared *NS* controlled *CS* corrosion effectively with inhibition efficacy 91% while the addition of *CdSe-NPs* to *NS* shifted the corrosion protection to higher value till touch 97%.

The main purpose of this study is to develop cost-effective and readily nonionic surfactant abundant with carbonyl, hydroxyl and propylene oxide groups with different ratios of *CdSe-NPs* which help in the stability and solubility of the prepared compound which was applied as efficient inhibitor for controlling *CS* corrosion in acidic solution using various chemical and electrochemical techniques. The existence of *CdSe-NPs* help enhanced inhibitor's solubility and *CS* surface coverage consequently enhanced the mitigation potency. Also, the surface-active parameters and effect of optical and dielectric parameters of the synthesized nonionic surfactant with and without variable concentrations of *CdSe-NPs* were evaluated and

---

*Corresponding author e-mail: mohamed.deefallah@feng.bu.edu.eg.; (Mohamed Deef Allah).

Receive Date: 20 January 2025, Revise Date: 12 February 2025, Accept Date: 05 March 2025
DOI: 10.21608/ejchem.2025.354271.11195

the interrelation features between the structural, dielectric and optical analysis were discussed to explore the possibilities of increasing the rate of corrosion inhibition efficiency via various techniques which makes the inhibition process very attractive.

2. Materials and Methods

2.1 Materials

The chemicals employed in the synthesis of *CdSe-NS* such as Cetyl bromide (mass fraction purity ≥ 98%), diethanolamine (mass fraction purity ≥ 98%) and propylene oxide (mass fraction purity ≥ 99%), Cadmium oxide (CdO 99.99%), trioctylphosphine oxide (TOPO 99.99%), Selenium (Se 99%), Hexadecylamine (HDA 98%), Oleic acid (≥99%), and Marcaptio proponic acid (MPA≥ 98%) were obtained from Sigma-Aldrich. Potassium hydroxide (mass fraction purity ≥ 98%) and all solvents were obtained from (ADWIC chemicals company, Egypt). Trioctyiphosphine (TOP 97%) was purchased from Fluka.

2.2 Inhibitors preparation and proposed techniques

CdSe-NS was prepared as shown in Scheme 1 as follows:

2.2.1 *Synthesis* of Nonionic Surfactant (*NS*)

Reaction mixture containing diethanolamine and cetylbromide in 1:1 molar ratio was dissolved in 20 ml of methanol/acetonitrile (30:70, v/v), and refluxed for 48 h in a water bath. The solvent was evaporated giving a white crystalline product (product-I: Cetyldiethanolammoniumbromide) which was washed with diethyl ether then recrystallized utilizing a mixed solvent of methanol/ethyl-acetate. The desired tertiary amine was obtained after dissolving product-I in 30 ml water and 30 ml of 2 N ammonia via extraction process with the addition of diethyl ether using separating funnel [17,18]. After that, 10 mmol of product-I was refluxed with 0.5 wt% KOH at 70 ºC in presence of N_2 (g) flow and dropwise addition of propylene oxide (PO) with vigorous mixing and warming under an efficient condensation process for about 12 h. After that, the reaction mixture was cooled to obtain the desired *NS* [19]. The chemical structure of the prepared *NS* was confirmed using FTIR spectra as in Fig.1 showing bands at 3385cm^{-1}, assigned to (OH) group, 2930 cm^{-1} ascribed to CH aliphatic, 1458 cm^{-1} C–H bond of CH_2 group, while the bands at 1271 $cm^{-1,}$ 1138 cm^{-1} and 1077 cm^{-1} were ascribed to C-O-C of ether group and 839 cm^{-1}[–(CH_2)n-] skeletal. While ^{1}HNMR in Fig.2 confirmed *NS* chemical structure showing different peaks at δ = 0.836 ppm (t, 3H, $\mathbf{CH_3}$), 1.027 ppm (d, 6H, $\mathbf{CH_3}CHOH$), 1.22 ppm (m, 26H, $CH_3(\mathbf{CH_2})_{13}$), 2.49 ppm (t, 4H, $OCH_2\mathbf{CH_2}$-N-$\mathbf{CH_2}CH_2O$), 3.14 ppm (t, 2H, $N\mathbf{CH_2}(CH_2)_n$), 3.23 ppm – 3.55 ppm (m, 8H, ether group: $\mathbf{CH_2}O\mathbf{CH_2}$), and 4.6 ppm (s, 2H, O**H**).

2.2.2 Synthesis of CdSe-Nanoparticles (*CdSe-NPs*)

Organometallic method was used for *CdSe-NPs* preparation as in the previously published work [20]. *CdSe-NPs* optical transmittance spectra were verified via a Uvikon 810 UV–Visible spectrophotometer and also, Philips EM400T electron microscope was used for TEM**.**

2.2.3 Synthesis of inhibitors (*CdSe-NS*)

For *CdSe-NS* preparation, 5 ml of *NS* solution (1×10^{-3} M) was mixed with (1%, 2%, 3% and 4 wt %) concentration of *CdSe-NPs* for 20 min, then the mixtures were stirred continuously for 2 h as in Scheme 1.

2.3 Surface tension measurements

Surface tension of the freshly prepared *NS* solutions in 1 M HCl at 25° C was measured using Kruss-K6 tensiometer. Surface parameters such as: critical micelle concentration (CMC), surface tension at CMC (γ_{cmc}), effectiveness (π_{cmc}), minimum surface area per molecule (A_{min}) and maximum surface excess concentration (Γ_{max}) at the air/solution interface were assessed and discussed.

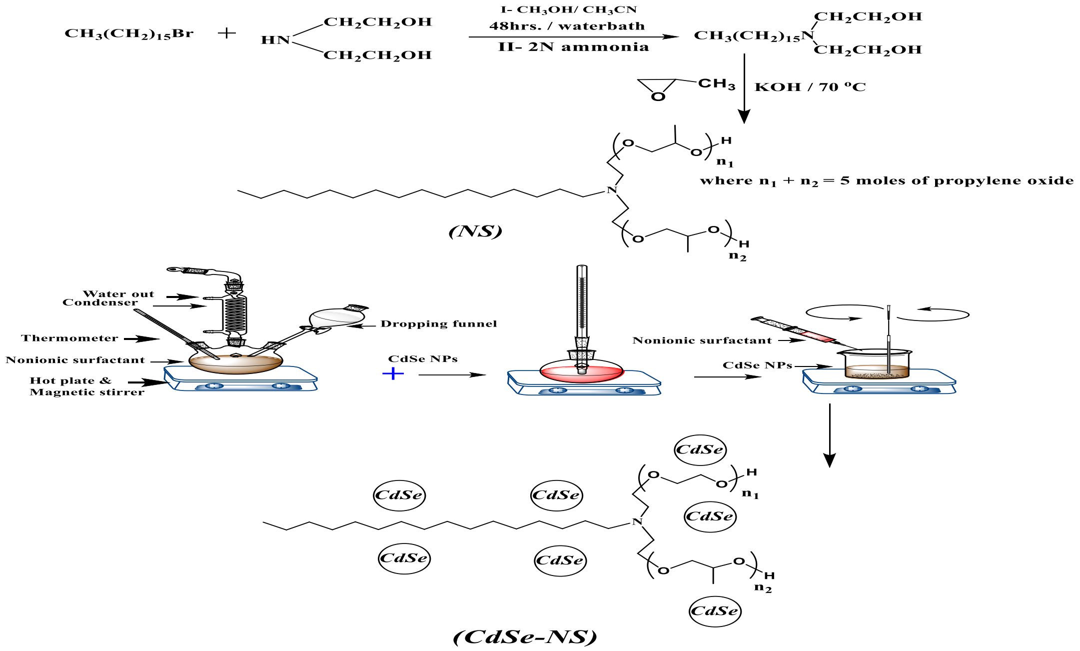

Scheme 1: ***Preparation process of CdSe-NS***.

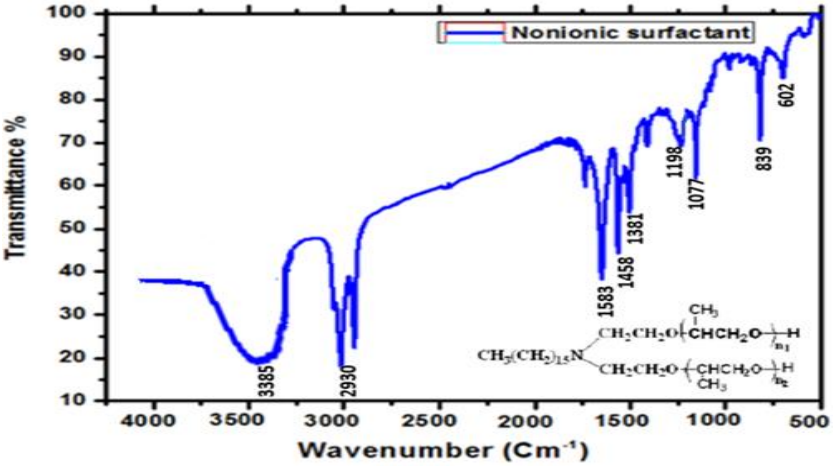

Fig.1: FTIR spectra of the prepared *NS*.

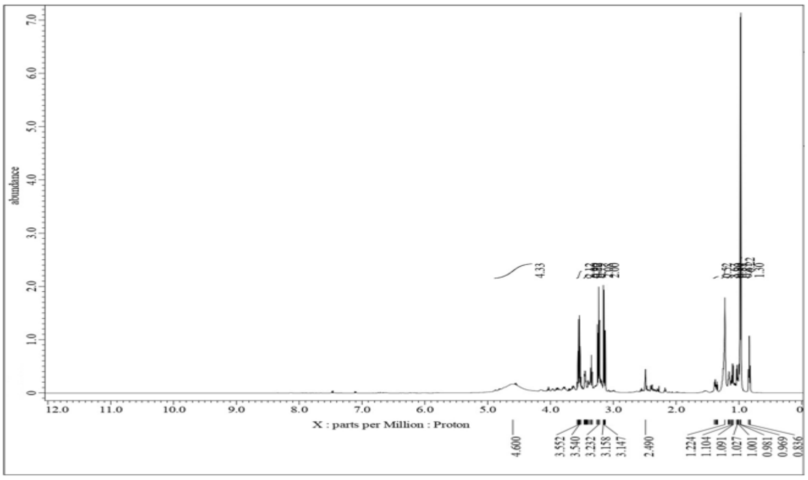

Fig.2: ^{1}HNMR of the prepared *NS*.

2.4 Corrosive solution and inhibitors

The aggressive solution (1 M HCl) was prepared by diluting the concentrated chemically pure 37% HCl grade acid with distilled water. In addition, various concentration (1*%wt* - 4*%wt*) of the prepared of *CdSe-NS* and *0%wt-CdSe-NS* (1×10^{-3} M of NS) in 1 M HCl solution were applied for evaluation *CS* corrosion behaviour at room temperature.

2.5 Weight Loss measurements (W_L)

CS samples with chemical composition in wt.%:(0.11% C, 0.45% Mn, 0.04% P, 0.05% S, 0.25% Si, and Fe balanced) were cut into suitable dimensions to fit W_L measurements and weighed before and after immersion in 1 M HCl solution with and without various concentration of *CdSe-NS* at room temperature for 6 h.

2.6. Electrochemical Techniques

Electrochemical measurements, including PDP and EIS, were performed using a computer-controlled potentiostat/galvanostat (Origalys) using a platinum electrode as counter electrode (CE), WE (Working Electrode, *CS*) and RE (Reference Electrode, Ag/AgCl, 3 M KCl). After OCP (Open Circuit Potential), EIS was performed using AC signals with an amplitude of 5 mV and a measuring frequency variation ranging from 100 kHz to 50 mHz. While PDP was measured at potential range ± 400 mV (vs. OCP) with a scan rate of 1 mVs^{-1}.

2.7 Surface analysis

The surface morphology of *CS* was investigated via atomic force microscopy (AFM) using Park System XE- 100 Atomic Force Microscope for 2D and 3D images of *CS* surface in absence and presence of the prepared inhibitor after 6 h of immersion.

3 Results and Discussions

3.1 Surface tension measurements

Surface tension (γ) and –log concentration (C) of the prepared *NS* relationship at 25 °C can be seen in Fig.3. As observed, the surface tension values decreased gradually with the increase of *NS* concentration which can be explained by accumulation of *NS* molecules at the air/liquid interface until there was no discernible change in surface tension value [21,22]. The graphically determined CMC by interacting the linear parts of the charted (γ) versus – log C curve is summarized in Table 1. Surface active properties effectiveness (Π_{cmc}), surface excess (Γ_{max}), and the average area occupied by single nonionic surfactant molecule (A_{min}) at water/air interface are calculated using the following equation [22–24]:

$$.\pi_{cmc} = \gamma_0 - \gamma_{cmc} \qquad (1)$$

Where (γ_0) denotes pure water's surface tension and (γ_{cmc}) the surface tension of *NS* at CMC.

$$\Gamma_{\max} = -\frac{1}{2.303\mathrm{nRT}}\left(\frac{\delta\gamma}{\delta\log\mathrm{C}}\right)_{\mathrm{T}} \qquad (2)$$

where Γ_{max} is the excess of the saturation of the surface - active ions, *R* is the gas constant, *T* is the temperature, and *n* is the number of solution species. (n= 1). As seen, the surface excess concentration of the prepared *NS* reduced as the hydrophobic portion of its length accumulated. The minimum surface area per adsorbed molecule, $\boldsymbol{A_{min}}$(nm^2), is the area in nm^2 occupied by each molecule at the liquid/air interface. A_{min} was determined by using the following equation [25]:

$$A_{min}=10^{16}/\Gamma_{max} N_A \qquad (3)$$

Where, N_A is the Avogadro's constant 6.023x10^{23}. The A_{min} value in Table 1 reflected that, *NS* molecules occupied high surface area at the interface; owing to the presence of carbon chain lengths which also, indicates that, the prepared *NS* has adsorption affinity at the interfaces and its ability to be used as a corrosion inhibitor [26].

Table 1: Surface active parameters of the prepared *NS* at 25 °C.

Comp.	**(mN/m)γ_{cmc}**	**π_{cmc} (mN/m)**	**CMC x10^{-3} (mol/dm^3)**	**$_{max}$ x10^{-10}Γ (mol cm^2)**	**A$_{min}$ (nm^2/mol)**
NS	33.45	38.55	2.679	1.2	138.02

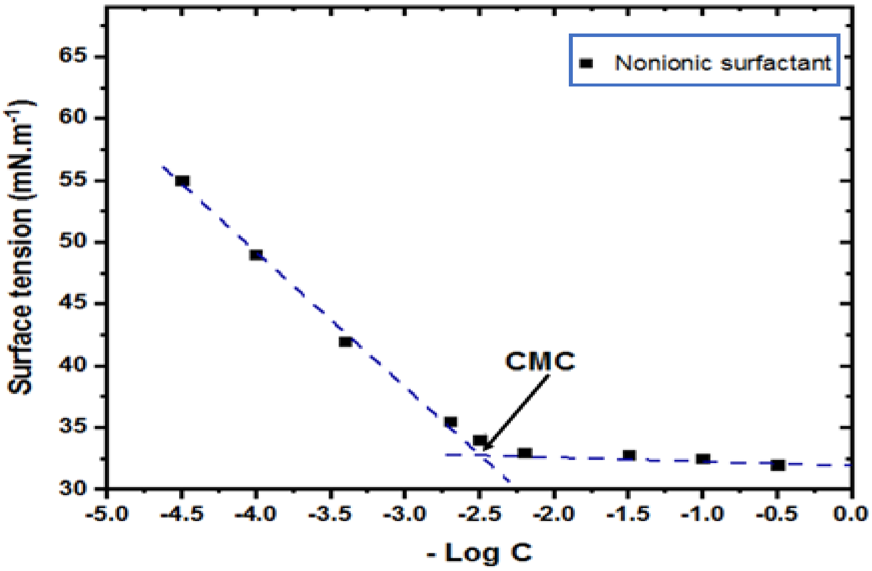

Fig.3: Surface tension vs. -log concentration of the synthesized *NS*.

3.2 Characterization of CdSe-NPs

The formation of *CdSe-NPs* was confirmed using absorption spectra in UV-vis region at wavelength range of 500 – 650 nm as seen in Fig.4(a). It was noticed that, an absorbance peak at 575 nm that supported *CdSe-NPs* formation due to their surface plasmon absorption clusters. The band gap energy (E_g) was determined by using the following equation [26,27].

$$\alpha\, h\, v = A(hv\text{-}E_g)^n \qquad (4)$$

The proper fit was found for *n* = ½, that implies the state of indirect optical transition. Fig.4 (b), display the relation between $(\alpha hv)^2$ against *hυ* for the *CdSe-NPs* showing E_g value with 1.96 eV which exhibited the ability of *CdSe-NPs* application as visible light photo catalyst in organic pollutant degradation. Also, transmission electron microscope (TEM) was utilized to scrutinize the morphological structure of *CdSe-NPs* as seen in Fig.4 (c, d). The selected area of electron diffraction (SAED) pattern indicates ring patterns with intense spots showing that the *CdSe-NPs* is polycrystalline as seen in Fig.4 (e). The particle size histogram seen in Fig.4 (f) has been magnified to facilitate measuring the average particle size by using the effective mass approximation method model applying the following equation [28]:

$$E_{gn} = E_{gb} + \frac{h^2}{8R^2}\left[\frac{1}{m_e} + \frac{1}{m_h}\right] - \frac{1.8e^2}{4\pi\varepsilon\varepsilon_0 R} \qquad (5)$$

The obtained value of average crystalline size of *CdSe-NPs* is found to be 4.70 nm with small spherical nanoparticles (rice like structure) and small agglomeration as noticed in TEM images which matched with that estimated from EMA.

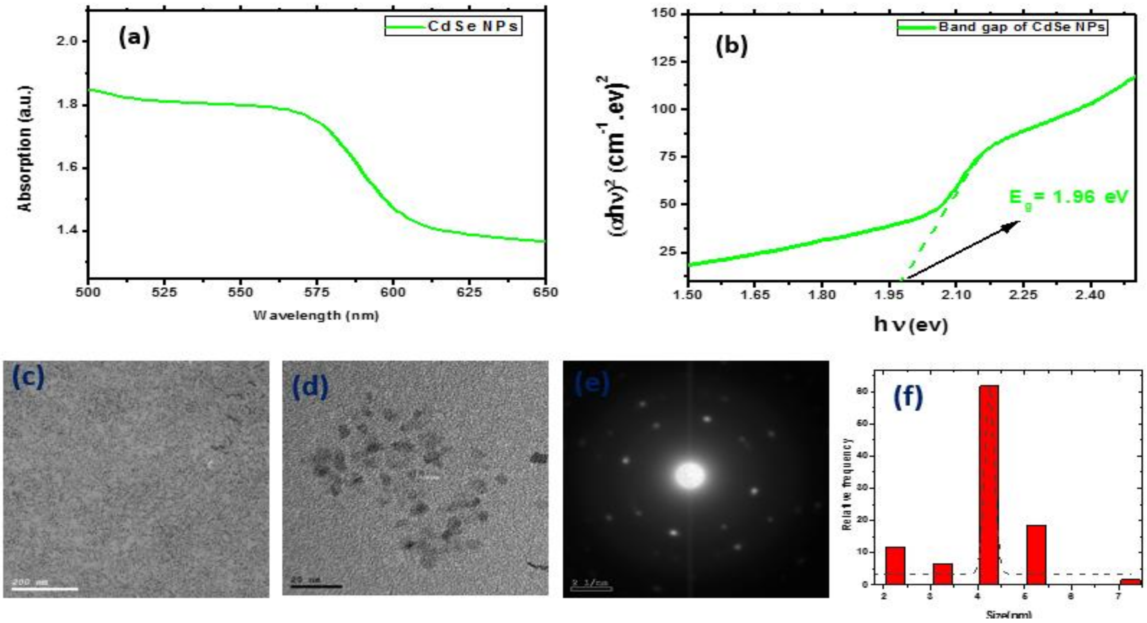

Fig.4: (a and b) UV-vis absorption and Tauc's plot versus wavelength for *CdSe-NPs* respectively, (c and d) TEM analysis of particle size with low and high magnification, (e) SAED pattern of (f) histogram distributions.

3.3 Corrosion studies

3.3.1 Weight Loss (W_L)

W_L is a simple way to determine corrosion rate (*CR*) of *CS* in 1 M HCl and after addition of different doses of *CdSe-NS*. The inhibition efficiency (η) and *CR* (g/cm^2.h), surface coverage (θ) and inhibition efficiency (η_{W_L}%) were calculated using the following equations [29]:

$$CR = \frac{\Delta W_1 - \Delta W_2}{20.71 \times t} \qquad (6)$$

$$\theta = \frac{\Delta W_1 - \Delta W_2}{\Delta W_1} \qquad (7)$$

$$\eta = \theta \times 100 \qquad (8)$$

Where, 20.71, t , ΔW_1 and ΔW_2 are *CS* surface area, immersion time (h) and the weight loss values without and with *CdSe-NS* respectively [30]. The data reported in Table.2 show that *CR* value decreases as the concentration of *CdSe-NS* in HCl increases which indicates that the maximum surface protection is found to be 0.97% at *4%wt-CdSe-NS*. This can be explained by the adsorption of *CdSe-NS* inhibitor on *CS* surface via their active sites such as hetero atoms (O and N) forming coordination bond with metal surface [31,32]. This finding demonstrated that, *CS* surface become obstructed by the adsorbed *CdSe-NS* molecules which behave as a protective barrier layer between *CS* and the corrosion surrounding [33]. From table, η value was 111 and 111 in presence of *0%wt-CdSe-NS* and *4%wt-CdSe-NS* respectively. This confirmed the defensive role of *CdSe-NPs* in *CS* protection via coverage and blocking extra *CS* surface area against the destructive attack of HCl solution [34]. The adsorbed film stability of *CdSe-NS* inhibitor over *CS* surface was studied using W_L measurements in absence and presence of the optimum concentration of (*4%wt-CdSe-NS*) at different temperature. Thermal film stability of *CdSe-NS* inhibitor studied at various temperature (25 ºC – 55 ºC) after 6 h immersion time. The computed data in Table 3 revealed that, a slight decline in the inhibition efficiency can be explained by a decrease in the adsorption capacity of *4%wt-CdSe-NS* as the temperature increases. Also, the mitigation potency of *4%wt-CdSe-NS* decreased slightly from 97 % at 25 °C till touch 95.92 % at 55 ºC which can be attributed to physical adsorption[35,36]. These annotations reflected the ability of the prepared *GCs-O* and *GCs* to inhibit the corrosion process of *CS* effectively at various temperature via their adsorption forming an insulation layer between *CS* surface and corrosive surrounding [37,38].

Table 2: Effect of inhibitors concentration on *CS* corrosion in 1 M HCl solution.at 25°C.

Conc.	W_t loss (gm)	θ	*IE%*
Blank	4.01	--	--
0%wt-CdSe-NS	0.35	0.91	91
1%wt-CdSe-NS	0.28	0.93	93
2%wt-CdSe-NS	0.20	0.95	95
3%wt-CdSe-NS	0.18	0.96	96
4%wt-CdSe-NS	0.13	0.97	97

Table 3: **Weight loss parameters for *CS* in absence and presence of *4%wt-CdSe-N* at different temperature.**

Inh.	**25 °C**			**35 °C**			**45 °C**			**55 °C**		
	Δ*w*, g	***θ***	***IE%***	**Δ*w*, g**	***θ***	***IE%***	**Δ*w*, g**	***θ***	***IE%***	**Δ*w*, g**	***θ***	***IE%***
Blank	4.01	----	----	5.934	----	----	8.715	----	----	12.234	----	----
4%wt-CdSe-NS	0.13	97	97	0.214	0.963	96.39	0.382	0.956	95.61	0.499	0.959	95.92

3.3.2 Potentiodynamic Polarization (PDP)

PDP curves of *CS* reaction in HCl free and after addition of various doses of *CdSe-NS* inhibitor were represented as in Fig.5. The similar PDP response of *CS* in absence and even after addition different doses from *CdSe-NS* confirmed that, *CS* reaction mechanism did not change. The addition of *CdSe-NS* shifted PDP curves to less active region which confirmed its inhibition role [39]. In addition, the observed parallel cathodic lines shown in Fig.5 reflected that the corrosion reaction mechanism and H_2 reduction reaction of *CS* were not affected by the introducing of *CdSe-NS* [40]. Some corrosion parameters like corrosion potential (E_{corr}), anodic and cathodic Tafel slopes (β_a and β_c), and η in Table 4 were calculated based on current density (i_{corr}) value according to the equation:

$$\eta = (i_{\mathrm{corr.blank}} - i_{\mathrm{corr.}inh})/i_{\mathrm{corr.blank}}) \times 100 \qquad (9)$$

Where $i_{\mathrm{corr.blank}}$ *and* $i_{\mathrm{corr.inh}}$ are the current density of *CS* in absence and presence of *CdSe-NS*, respectively [41]. The data reported in Table 4 showed the mitigation power of *CdSe-NS* inhibitor for *CS* in destructive HCl solution. It was noticed that, value of i_{corr} decreases after addition of *CdSe-NS* inhibitor owing to blocking of both cathodic and anodic regions through *CdSe-NS* adsorption process[42]. The change in E_{corr} values was less than 85 mV as noticed in Table 4 revealed that, *CdSe-NS* inhibitor behaved as mixed-type inhibitor [43–45]. In addition, the slightly variation in both β_a and β_c values signifying that *CS* corrosion mechanism not modified by the addition of *CdSe-NS* [46]. Moreover, it can be noticed from Table 4 that the addition of *CdSe-NS* inhibitor shifted the values of R_p and i_{corr} to higher and lower values, respectively. This can be explained by shielding of *CS* surface against the corrosive particles via construction of barrier layer which increase the resistance of *CS* to be corroded [47]. The value of η in Table 4 increased to 91.88% % and 96.26% in presence of *0%wt-CdSe-NS* and *4%wt-CdSe-NS*, respectively. The data obtained from Table 4 reinforced the role of *CdSe(NPs)* in *CS* protection which can be clarified by the blocking effect of *CdSe(NPs)* which increases *CS* surface coverage against the corrosive surrounding. All these observations confirmed the adsorption behaviour of *CdSe-NS* inhibitor and its significant role in *CS* protection.

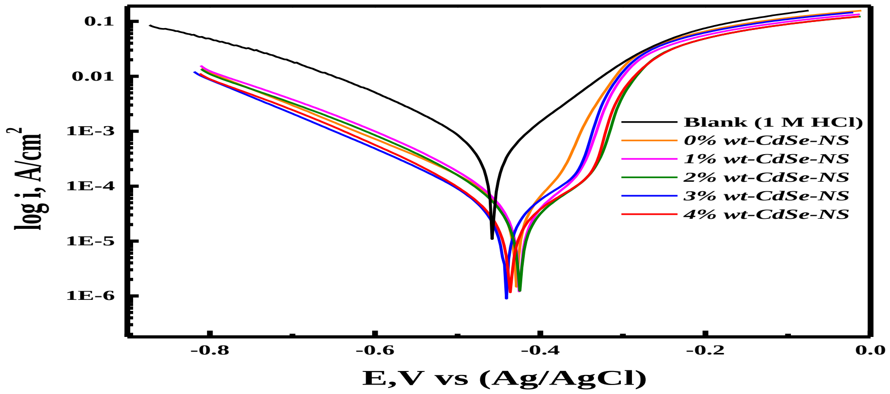

Fig.5. Potentiodynamic Polarization curves of *CS* in 1 M HCl and after addition of various does of *CdSe-NS* at room temperature.

Table 4: PDP data of *CS* in 1 M HCl free and after addition of various doses of *CdSe-NS* at room temperature.

Conc.	E_{corr}, (V)	β_a (V/dec)	$-\beta_c$ (V/dec)	i_{corr} (A/cm²)	*CR* (mm/year)	R_P (Ω.cm²)	θ	*IE%*
Blank	-0.457	0.1029	0.1494	51.51E-05	6.121	40.98	------	------
0%wt-CdSe-NS	-0.428	0.0928	0.1601	4.18E-05	0.485	428.49	0.9188	91.88
1%wt-CdSe-NS	-0.424	0.0861	0.1037	3.19E-05	0.374	723.46	0.9381	93.81
2%wt-CdSe-NS	-0.441	0.0789	0.1404	2.67E-05	0.309	823.09	0.9482	94.82
3%wt-CdSe-NS	-0.424	0.0892	0.1285	2.13E-05	0.252	917.64	0.9586	95.86
4%wt-CdSe-NS	-0.436	0.0884	0.1396	1.92E-05	0.225	1057.31	0.9626	96.26

3.3.3 Electrochemical Impedance Spectroscopy (EIS)

EIS technique was applied for studying the corrosion behavior of *CS* in 1 M HCl free and containing various doses of the prepared *CdSe-NS* at room temperature. The imperfect semicircle shape of Nyquist plot shown in Fig.6 may be attributed to the *CS* roughness, inhomogeneity, and distribution of active sites (frequency dispersion phenomenon) [48]. The addition of *CdSe-NS* inhibitor forms a defensive layer over *CS* surface which obstructs the ionization of *CS* which can be observed as in Nyquist diameter enhancement in to higher values [49,50]. The appearance of Nyquist arcs in absence and presence of *CdSe-NS* seems to be identical with variation in their capacity besides Bode-phase diagram in Fig.7 with one time constant at *0%wt-CdSe-NS*. The *CS* corrosion mechanism, controlled by mass transfer with proposed equivalent circuit (EC) in Fig.8, consists of R_s (solution resistance), *CPE* (constant phase element) can be defined by Y_o, coefficient n and R_p (polarization resistance) which involved R_{ct} (charge transfer resistance) [51–53]. At higher concentrations (*1%wt-CdSe-NS* to *4%wt-CdSe-NS*), two time constant was detected indicating that *CS* corrosion mechanism changed owing to stable adsorbed film formation with proposed EC in Fig.8 comprised of R_s *CPE* and R_p (= R_{ct} + R_f "film resistance")[54]. The observed dropping in *n* values reported in Table 5 can be explained by current arises distribution from surface roughness which reflected that surface heterogeneity increased by the adsorption of adsorbed *CdSe-NS* over *CS* surface.[55,56]. The Y° values decreased with *CdSe-NS* addition due to the replacement process of the corrosive particles with *CdSe-NS* molecules consequently increase the thickness (*T*) of adsorbed layer over *CS* surface[57,58]. Based on Helmholtz equation, the value of C_{dl} (double layer capacitance) decreased with *CdSe-NS* addition as the following equation [59]:

$$C_{\mathrm{dl}} = \left(\frac{\varepsilon^{\circ}\varepsilon}{T}\right) A \qquad (10)$$

Where A, ε° and ε are *CS* surface area, air and local dielectric constant [60,61]. η was calculated based on Rp value according to the following equation:

$$\eta = (R_{P.Inh} - R_{P.blank})/R_{P.\ Inh})\ X100 \qquad (11)$$

Where $R_{P.Inh}$ and $R_{P.blank}$ are polarization resistance in presence and absence of inhibitor. The rising of R_P values in Table 5 reflecting the inhibition effect of the prepared *CdSe-NS*. R_P increased to touch 1061.4 Ω.cm^2 in presence of *4%wt-CdSe-NS* relative to free HCl 36.55 Ω.cm^2. In addition, η values in Table 5 are 91.59% and 96.55% in presence *0%wt-CdSe-NS* and *4%wt-CdSe-NS*, respectively. This bolstered the role of *CdSe-NPs* in *CS* protection which can be explained by more *CS* surface coverage and blocking film pores which enhanced the mitigation potency for *CS* [62,63]. The data of W_L, EIS and PDP were in good agreement with each other.

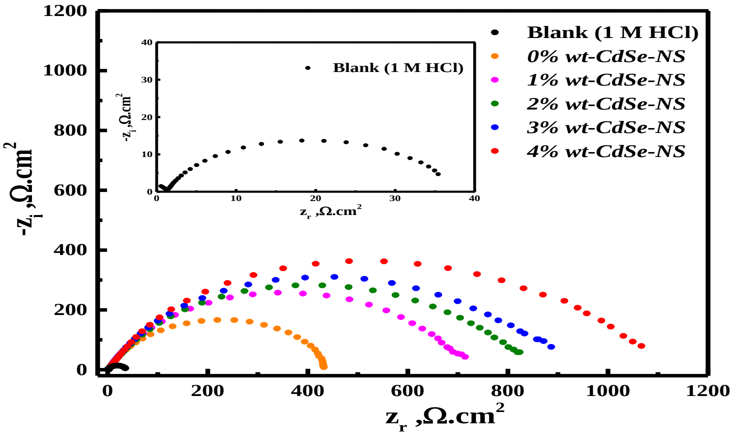

Fig.6: Nyquist plots of *CS* in 1 M HCl and after addition of various does of *CdSe-NS* at room temperature.

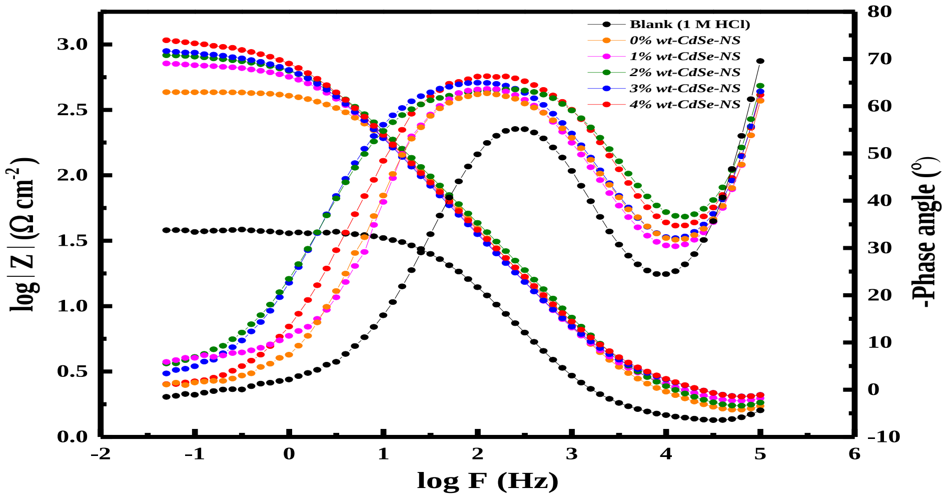

Fig.7: Bode-Phase plots of *CS* in 1 M HCl and after addition of various does of *CdSe-NS* at room temperature.

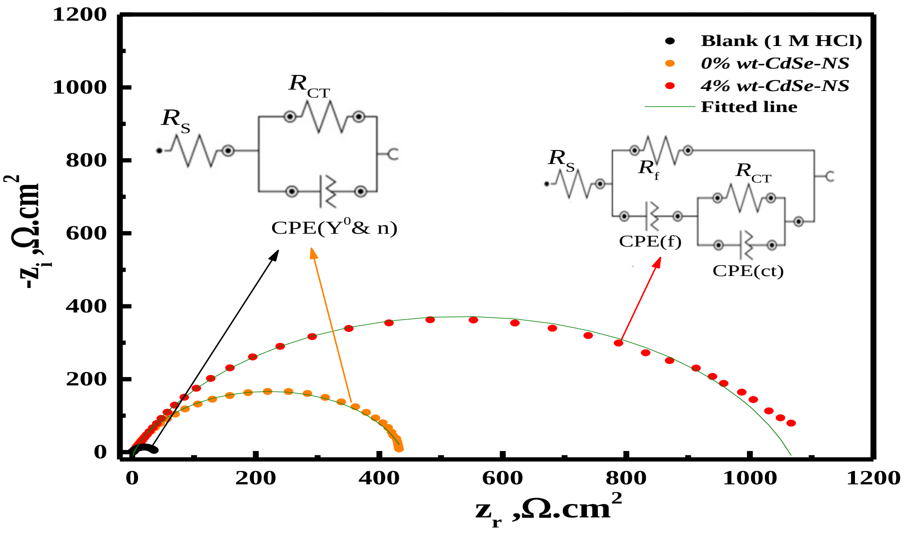

Fig.8: **Fitted EIS experimental data using the equivalent circuit for *CS* in 1 M HCl in absence and presence of *0%wt-CdSe-NS* and *4%wt-CdSe-NS*.**

Table.5: **EIS parameters for *CS* in 1 M HCl in absence and presence of various doses of *CdSe-NS* at temperature**.

Conc.	R_S (Ω.cm2)	CPE		R_{Ct} (Ω.cm^2)	R_f (Ω.cm^2)	θ	*IE%*
		Y^o Ω^{-1} cm^{-2} x10^{-5}	n				
Blank	1.45	9.89	0.827	36.55	---	---	---
0%wt-CdSe-NS	3.57	7.38	0.831	434.98	---	0.9159	91.59
1%wt-CdSe-NS	2.35	8.65	0.794	710.07	3.82	0.9488	94.88
2%wt-CdSe-NS	1.33	6.83	0.768	820.18	5.41	0.9557	95.57
3%wt-CdSe-NS	1.45	6.15	0.764	911.6	9.73	0.9603	96.03
4%wt-CdSe-NS	2.32	5.13	0.778	1049.05	11.35	0.9655	96.55

3.4 Optical characterization of CdSe-NS

3.4.1 Optical dielectric function (DF)

The magnitude of the optical dielectric constants of the *CdSe-NS* at different doses of *CdSe-NPs* were evaluated via the following equation [64–66]:

$$\acute{\varepsilon} = n^2 - k^2 \qquad (13)$$

$$\varepsilon'' = 2nk \qquad (14)$$

where $\acute{\varepsilon}$, ε'' are real and imaginary parts of dielectric constants, respectively. Fig.9(a,b) presents the variation of the values of real and imaginary parts of both $\acute{\varepsilon}$ and ε'' versus wavelength at different percentage of *CdSe-NPs*. It can be seen from Fig.9(a, b), both $\acute{\varepsilon}$ and ε'' increase with the increase of *CdSe-NPs* percent. Also, the value of $\acute{\varepsilon} > \varepsilon''$ which can be attributed to the strong dependence of $\acute{\varepsilon}$ on the refractive index while ε'' value depends on the extinction coefficient values which are related to the variation of the absorption coefficient [67]. The dielectric loss factor *Tan(δ)* is a valuable factor for investigating the structure defects owing to energy loss and can be determined according to the following equation [68]:

$$Tan(\delta) = \varepsilon'' / \varepsilon' \qquad (15)$$

It is obvious that, *Tan(δ)* increased with the increase of *CdSe-NPs* as seen in Fig.9(c) as a result of the abrupt rise in the absorption coefficient, besides nearly constant dependence was observed at higher wavelength and a strong dependence at lower wavelength [69]. The complex electrical modulus *(M)* is utilized in the analysis of dielectric and electrical conductivity behavior [70]. *M* was initiated from the dielectric constants using the following equation [71]:

$$M = \frac{\varepsilon'}{(\varepsilon')^2 + (\varepsilon'')^2} \qquad (16)$$

As in Fig.9(d). *M* was very close to zero at small wavelength while the magnitude of *M* increased with wavelength rising. Besides, the position of the complex electrical modulus peaks shifted towards higher wavelength and then reaches a constant value after a specific wavelength with the increase of *CdSe-NPs* doses. All these results showed that the conduction mechanism and the behavior of the dielectric parameters are enhanced and improved with the rising *CdSe-NPs* concentration [72,73].

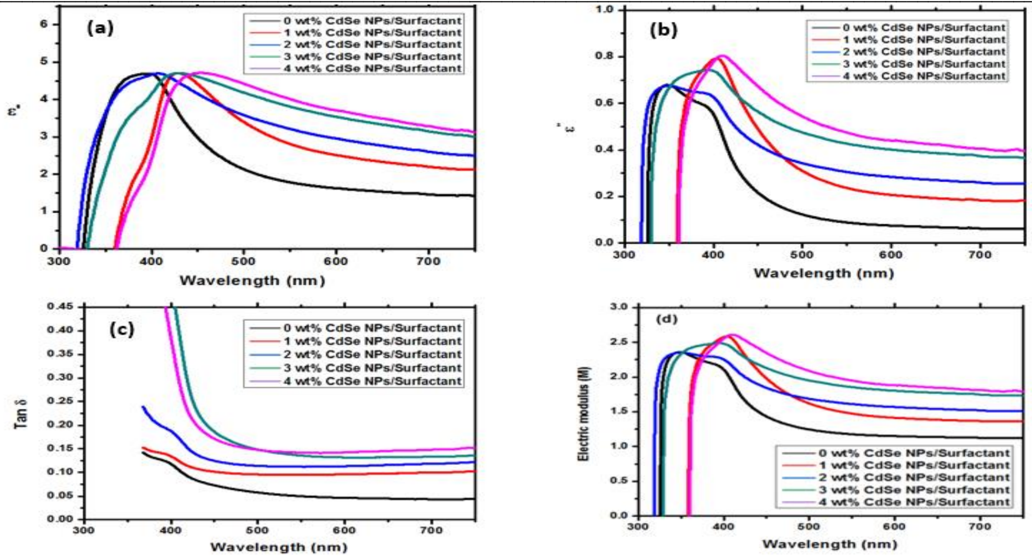

Fig.9: (a-d) presents variation of έ and ε'', Variation of the dielectric loss (Tan δ), the electric modulus (M) curve respectively vs. wavelength of the prepared samples.

3.4.2 Dispersion parameters (n&k).

Fig.10(a, b) show the optical absorbance and the transmittance spectra for the prepared *CdSe-NS* with different doses of *CdSe-NPs* as a function of wavelength (λ) range from (300–750) nm. Fig.10(a) shows an increasing trend in the optical absorbance with *CdSe-NPs* concentration increases which reflects a good complexation between the nanoparticles. Fig.10(b) indicates the transmission spectra of the *CdSe-NS* with a maximum of 85%. In addition, a reduction in the transmittance is noticed with the increase of *CdSe-NPs* concentration owing to the optical energy gap. Therefore, the transmission decreases while the absorption increases. The absorption coefficient (α) can be calculated for the *CdSe-NS* by applying the following equation [28,74]:

$$\alpha = 2.303\ A/T \qquad (12)$$

Where (A) is the absorbance and (T) is the film thickness[74,75]. Fig.11(a) presents the absorption coefficient of *CdSe-NS* with different *CdSe-NPs* wt% as a function of photon energy ($h\upsilon$). As noticed, the absorption coefficient increases with increasing *CdSe-NPs* ratio which can be attributed to rising of *NS* interaction with *CdSe-NPs* and means that there is a large probability of allowed direct transition [76,77]. The optical energy gap values can be estimated by Tauc´s equation mentioned earlier in Section (3.3) as shown in Fig.11(b). As seen the linear portion of the graph gives the value of the direct optical energy gap (E_g). The variation of E_g value increased from 3.35 to 3.82 eV with *CdSe-NPs* concentration as clearly seen in Fig.11(c) can be explained by *CdSe-NPs* surface and interface effect with *NS* which includes surface roughness that caused a change in refractive index consequently changed the band gap. Therefore, the addition of *CdSe-NPs* enhanced the adsorption capacity of *NS*. All these observations confirmed that the existence of *CdSe-NPs* increased the inhibition efficiency of the prepared inhibitor [78,79]. Refractive index (n) and extinction coefficient (k) are important parameters that help in computing the dielectric constants of the materials. n and k value can be calculated using the equations given in details in [80,81], and are presented in Fig.12(a,b) as a function of wavelength showing enhancement in n with *CdSe-NPs* doses at higher wavelength which can be attributed to the increase of the free carriers and the reflection in *CdSe-NS*, besides a decline in propagation velocity of light resulting in the increase of n value. Also, the rising of k value with *CdSe-NPs* content increases the optical energy gap as a result of absorbance increment. This fact suggested that, the photon energy unable to excite electrons due to reflection and hence k value increase[82,83].

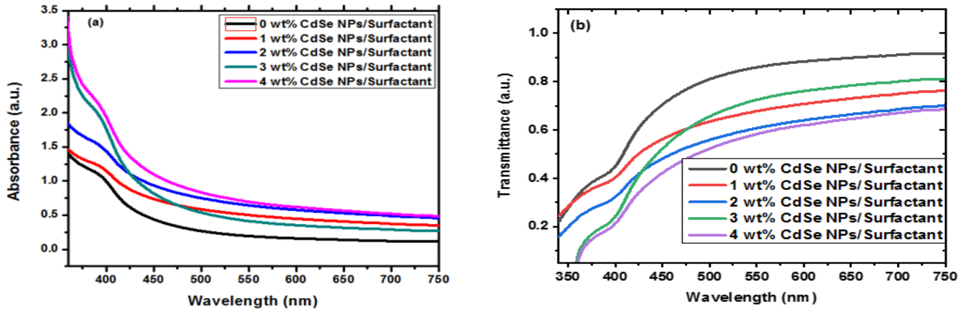

Fig.10: (a and b) The optical absorbance and transmittance spectra vs. wavelength of *CdSe-NS* with different concentration of *CdSe-NPs*

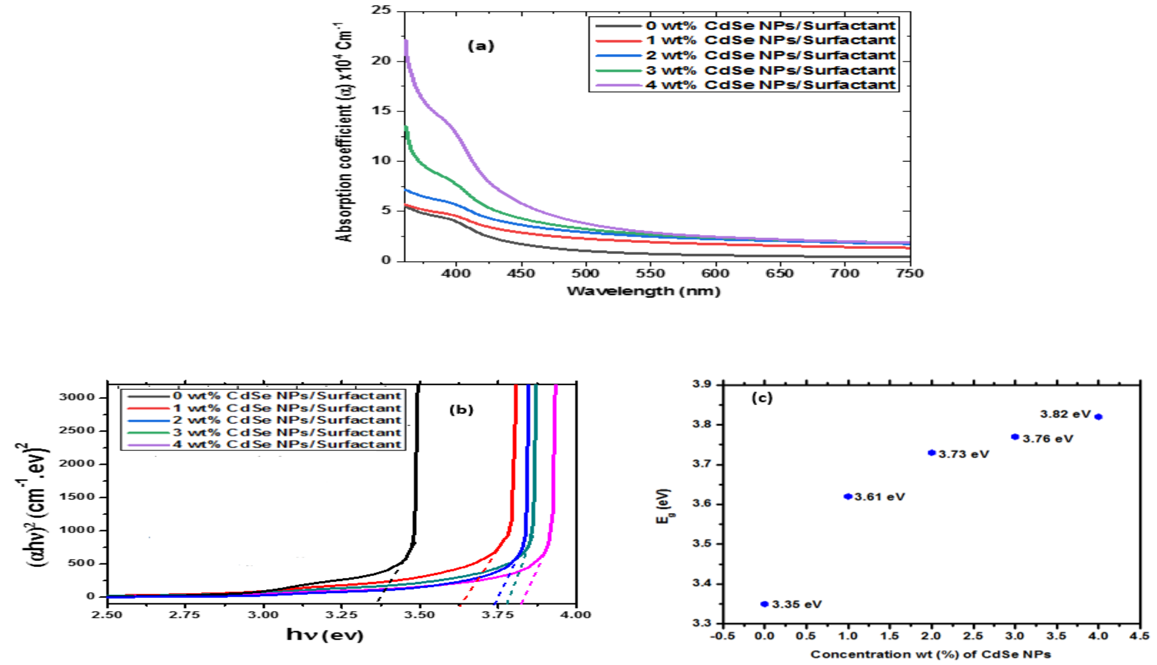

Fig.11: (a) Dependence of the absorption coefficient (α) versus wavelength, (b) dependence of $(\alpha h\upsilon)^2$ on the photon energy (hυ), and (c) the relation between concentration of *CdSe-NPs* in surfactant with bandgap E_g.

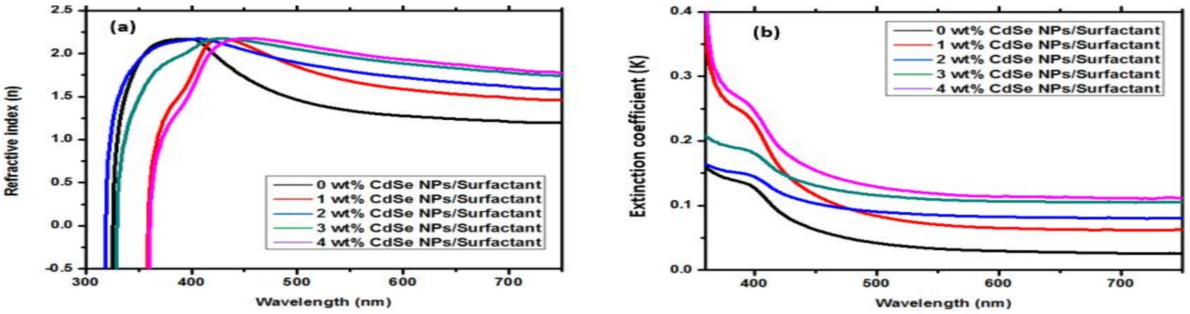

Fig.12: (a and b) The refractive index (n) and the extinction coefficient (K) curve versus wavelength of *CdSe-NS* with different concentration of *CdSe-NPs.*

3.5 Atomic Force Microscope (AFM) evaluation

AFM is considered as a scientific method for identifying the topography of *CS* surface and determining changes in the morphological features of *CS* surface in 1 M HCl free solution and after treatment with *0%wt-CdSe-NS* and *4%wt-CdSe-N.* Fig.13 shows two-dimensional (2D) and three-dimensional (3D) images of *CS* surface in the uninhibited and inhibited solutions. The average *CS* roughness (R_a) in 1 M HCl free with 978.76 nm, exhibited that. the increase in the surface roughness can be attributed to the deterioration behaviour of HCl on the metal surface which can be observed as cracks and potholes in *CS* surface as in Fig.13 [84–86]. However, the addition of *0%wt-CdSe-NS* and *4%wt-CdSe-NS* showed a decrease in R_a value to 185.62nm and 142.56nm, respectively. This can be clarified by AFM images in Fig.13 showing a notable improvement in *CS* surface. This reflected the inhibition power of the prepared inhibitors via formation of an insulation barrier layer over *CS* surface against the corrosive environment[37,86,87].

Table 6 includes an overview of some articles on the use of different nanoparticles (NPs) and it's inhibition efficiency comparing with CdSe (NPs) to prevent corrosion in 1M HCl.

Table.6: some of the previous work on the corrosion inhibition of metals using different nanoparticles (NPs).

Different NPs.	*IE%*	*References*
Ag NPs	94.3	[88]
ZnO NPs	89.31	[89]
MgO NPs	76.2	[90]

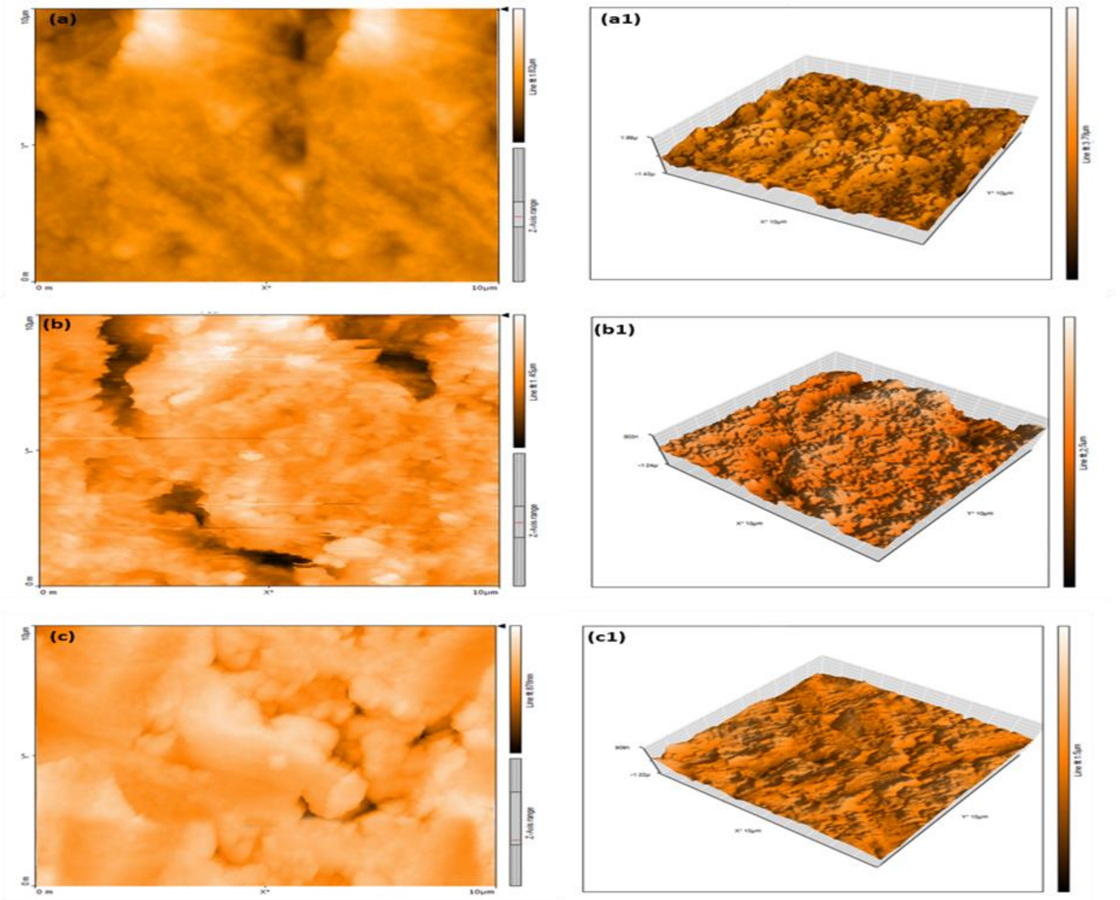

Fig.13: **2D and 3D AFM for *CS* surface after immersion in 1 M HCl free (a and a1) and after addition of *0%wt-CdSe-NS* (b and b1) and *4%wt-CdSe-NS* (c and c1).**

4. Conclusion

In the present study, *CdSe-NPs* were synthesized and added to *NS* in different concentrations for more *CS* corrosion control in 1 M HCl solution. The inhibition performance of the studied inhibitors (*NS* and *CdSe-NS*) was studied using various chemical and electrochemical measurements. The following conclusions can be summarized from the obtained data:

1. The chemical structure of the synthesized *NS* was characterized using ^{1}H NMR and FT-IR spectroscopy.
2. The formation of *CdSe-NPs* was characterized using UV-vis (ultraviolet) and TEM (transmission electron microscope).
3. W_L measurements confirmed the defensive role of *CdSe-NPs* in *CS* protection via blocking extra *CS* surface area against the destructive attack of HCl solution with inhibition efficiency 97 %.
4. The prepared *NS* shifted *CS* corrosion rate and current density (i_{corr}) values to lower values till reach 0.225 mm/year and 1.92×10^{-5} A/cm^2 respectively at 4%*wt-CdSe-NS.*
5. The addition of *CdSe-NPs* to *NS* exhibited more mitigation potency for *CS* and increased with rising of *CdSe-NPs* concentration till touch 96.55% using EIS at 4%*wt-CdSe-NS.*
6. A good correlation was obtained between the calculated values of the inhibition efficiency and those obtained from various techniques such as PDP and EIS.
7. The inhibition performance of the synthesized inhibitor was assessed at various temperatures using W_L measurements indicating that, the inhibition power of *CdSe-NS* with mitigation potency 95.92% at 55 °C.
8. The electronic structure, the optical, and dielectric properties were investigated in order to capture the influence of *CdSe-NS* behavior in the corrosive environments and its influence on the corrosion inhabitation rate of *CS*.
9. In addition, the inhibition power of the prepared inhibitors was confirmed using AFM via formation of an insulation barrier layer over *CS* surface against the corrosive environment.

Funding: This research received no external funding.

Conflicts of Interest: The authors declare no conflict

Acknowledgement
The opto-electrical parameters were measured at Laser Physics and Nanotechnology Unit (LPTU), Faculty of Engineering, Shoubra, Benha University**.**

References.

[1] Wu HY, Shih CL, Lee T, Chen TY, Lin LC, Lin KY, et al. Development and validation of an analytical procedure for quantitation of surfactants in dishwashing detergents using ultra-performance liquid chromatography-mass spectrometry. Talanta 2019;194:778–85. https://doi.org/10.1016/j.talanta.2018.10.084.

[2] Fouda AS, Khalil EM, EL-Mahdy GA, Shaban MM, Mohammed AS, Abdelsatar NA. Synthesis and characterization of novel acrylamide derivatives and their use as corrosion inhibitors for carbon steel in hydrochloric acid solution. Sci Rep 2023;13:1–16. https://doi.org/10.1038/s41598-023-30574-3.

[3] Mu'azu ND, Haladu SA, AlGhamdi JM, Alqahtani HA, Manzar MS, Zubair M, et al. Inhibition of low carbon steel corrosion by a cationic gemini surfactant in 10wt.% H2SO4 and 15wt.% HCl under static condition and hydrodynamic flow. South African J Chem Eng 2023;43:232–44. https://doi.org/10.1016/j.sajce.2022.10.006.

[4] Atta AM, Abdullah MMS, Al-Lohedan HA, Ezzat AO. Demulsification of heavy crude oil using new nonionic cardanol surfactants. J Mol Liq 2018;252:311–20. https://doi.org/10.1016/j.molliq.2017.12.154.

[5] Earnden L, Van Der Zalm J, Chen A, Marangoni AG, van Lier R, Pensini E. Comparative study of corrosion inhibition by three anionic surfactants in an acidic environment. J Surfactants Deterg 2022;25:399–411. https://doi.org/10.1002/jsde.12568.

[6] Hasheminejad M, Nezamzadeh-Ejhieh A. A novel citrate selective electrode based on surfactant modified nano-clinoptilolite. Food Chem 2015;172:794–801. https://doi.org/10.1016/j.foodchem.2014.09.057.

[7] Zhao Q, Li Y, Chai X, Zhang L, Xu L, Huang J, et al. Interaction of nano carbon particles and anthracene with pulmonary surfactant: The potential hazards of inhaled nanoparticles. Chemosphere 2019;215:746–52. https://doi.org/10.1016/j.chemosphere.2018.10.016.

[8] Al-Sabagh AM, Nasser NM, Khamis EA, Mahmoud T. Synthesis of non-ionic surfactants based on alkylene diamine and evaluation of their corrosion inhibition efficiency on carbon steel in formation water. Egypt J Pet 2017;26:41–51. https://doi.org/10.1016/j.ejpe.2016.03.001.

[9] Mobin M, Zehra S, Parveen M. L-Cysteine as corrosion inhibitor for mild steel in 1 M HCl and synergistic effect of anionic, cationic and non-ionic surfactants. J Mol Liq 2016;216:598–607. https://doi.org/10.1016/j.molliq.2016.01.087.

[10] Migahed MA, Farag AA, Elsaed SM, Kamal R, Mostfa M, El-Bary HA. Synthesis of a new family of Schiff base nonionic surfactants and evaluation of their corrosion inhibition effect on X-65 type tubing steel in deep oil wells formation water. Mater Chem Phys 2011;125:125–35. https://doi.org/10.1016/j.matchemphys.2010.08.082.

[11] Abd El Wanees S, Bukhari AAH, Alatawi NS, Khalil SA, Nooh S, Mustafa SK, Elyan SS .Thermodynamic and Adsorption studies on the corrosion inhibition of Zn by 2,2'-Dithiobis(2,3-dihydro-1,3 benzothiazole) in HCl Solutions, Egypt J Chem, 2021;547 – 559: 64(2).
DOI: 10.21608/EJCHEM.2020.42128.2849

[12] Shaban SM, Aiad I, El-Sukkary MM, Soliman EA, El-Awady MY. Synthesis of newly cationic surfactant based on dimethylaminopropyl amine and their silver nanoparticles: Characterization; surface activity and biological activity. Chinese Chem Lett 2017;28:264–73. https://doi.org/10.1016/j.cclet.2016.09.010.

[13] Huang B, Huang C, Chen J, Sun X. Size-controlled synthesis and morphology evolution of Nd2O3 nano-powders using ionic liquid surfactant templates. J Alloys Compd 2017;712:164–71. https://doi.org/10.1016/j.jallcom.2017.04.009.

[14] Du S, Chen S, Zhang Z, Ye Z, Mao H, Yang H, et al. Corrosion inhibition behavior of hydroxyl-terminated hyperbranched poly(amine-ester) for Q235 steel in HCl solution. Mater Chem Phys 2022;292:126831. https://doi.org/10.1016/j.matchemphys.2022.126831.

[15] Liu W, Zhang X, Qiang Y, Lu G, Lan X, Chen B, et al. Ureidopyrimidinone-containing Poly(amino ester) for corrosion inhibition of mild steel in acidic medium. Mater Chem Phys 2022;292:126818. https://doi.org/10.1016/j.matchemphys.2022.126818.

[16] Punitha N, Ganapathi Sundaram R, Vijayalakshmi K, Rengasamy R, Elangovan J. Interactions and corrosion mitigation prospective of pyrazole derivative on mild steel in HCl environment. J Indian Chem Soc 2022;99:100667. https://doi.org/10.1016/j.jics.2022.100667.

[17] Mishra BK, Mukherjee P, Dash S, Pa el S, Pati HN. Alkylation of ethanolamines: An approach to a novel class of functional surfactants. Synth Commun 2009;39:2529–39. https://doi.org/10.1080/00397910802656109.

[18] Mahgoub FM, Hefnawy AM, Abd Alrazzaq EH. Corrosion inhibition of mild steel in acidic solution by leaves and stem extract of acacia nilotica. Desalin Water Treat 2019;169:49–58. https://doi.org/10.5004/dwt.2019.24681.

[19] Hefnawy M El, Allah MD, Abd Elhamed S. New Biodegradable Nonionic-Anionic Surfactants Based on Different Fatty Alcohols as Corrosion Inhibitors for Aluminum in Acidic Medium. J Surfactants Deterg 2021;24:365–79. https://doi.org/10.1002/jsde.12473.

[20] Fouad SS, Easawi K, Mahmoud TS, Nabil M. Essential tips for enhancing the opto-electrical performance of CdSe (NPs)/Epoxy resin. J Non Cryst Solids 2023;608:122252. https://doi.org/10.1016/j.jnoncrysol.2023.122252.

[21] Bedir AG, Abd El-Raouf M, Abdel-Mawgoud S, Negm NA, El Basiony NM. Corrosion Inhibition of Carbon Steel in Hydrochloric Acid Solution Using Ethoxylated Nonionic Surfactants Based on Schiff Base: Electrochemical and Computational Investigations. ACS Omega 2021;6:4300–12. https://doi.org/10.1021/acsomega.0c05476.

[22] Abd El-Ghaffar MA, Sherif MH, Taher El-Habab A. Synthesis, Characterization, and Evaluation of Ethoxylated Lauryl-Myrisityl Alcohol Nonionic Surfactants as Wetting Agents, Anti-Foamers, and Minimum Film Forming Temperature Reducers in Emulsion Polymer Lattices. J Surfactants Deterg 2017;20:117–28. https://doi.org/10.1007/s11743-016-1898-4.

[23] Deef Allah M, Abdelhamed S, Soliman KA, El-Etre MA. The performance of three novel Gemini surfactants as inhibitors for acid steel corrosion: experimental and theoretical studies. RSC Adv 2021;11:37482–97.

---

https://doi.org/10.1039/d1ra07449k.

[24] El-Etre MA, Abdelhamed S, Allah MD. Synthesis of Novel Gemini Surfactants Based on Succinic Acid and Their Application as Inhibitors for Carbon Steel Corrosion. J Bio- Tribo-Corrosion 2020;6:1–12. https://doi.org/10.1007/s40735-020-00425-z.

[25] Adawy AI, Soliman RM, Dhmees AS, Abdeen ZI. Antimicrobial activity of polymeric surfactants blending with zinc oxide nanoparticles derived from Electric Arc Furnace Dust, Egypt J Chem. 2021; 64:2–3. DOI:10.21608/EJCHEM.2021.75608.3707

[26] Nabil M, Mohamed SA, Easawi K, Obayya SSA, Negm S, Talaat H, et al. Surface modification of CdSe nanocrystals: Application to polymer solar cell. Curr Appl Phys 2020;20:470–6. https://doi.org/10.1016/j.cap.2020.01.001.

[27] Fouad SS, Barádacs E, Nabil M, Sharma A, Mehta N, Erdélyi Z. Linearization and characterization of the Wemple – DiDomenico model of ZnO/Ni/ZnO tri-layer thin films prepared by ALD and DC magnetron sputtering. J Alloys Compd 2024;990. https://doi.org/10.1016/j.jallcom.2024.174348.

[28] El-Metwally EG, Assim EM, Fouad SS. Optical characteristics and dispersion parameters of thermally evaporated Ge50In4Ga13Se33 chalcogenide thin films. Opt Laser Technol 2020;131:106462. https://doi.org/10.1016/j.optlastec.2020.106462.

[29] Basiony NM El, Salim MM, Elaraby A, Elbalaawy AY, Nasser A, Migahed MA, et al. ρ -Substituted imine cationic surfactants as carbon steel corrosion inhibitors : Experimental and theoretical (DFT and MCs) approaches. J Mol Liq 2024;400:124475. https://doi.org/10.1016/j.molliq.2024.124475.

[30] Nasser AJA, Sathiq MA. ORIGINAL ARTICLE N - [Morpholin-4-yl (phenyl) methyl] acetamide as corrosion inhibitor for mild steel in hydrochloric acid medium. Arab J Chem 2011. https://doi.org/10.1016/j.arabjc.2011.07.024.

[31] Eldougdoug WI, Ali AI, Elaraby A, Mabrouk EM. Corrosion inhibition of Tri-cationic surfactant on carbon steel in hydrochloric acid solution 2018;5:289–300.

[32] Mohini GJ, Krishnamacharyulu N, Baskaran GS, Srinivasa C, Kumar VR, Veeraiah N. In fl uence of strontium on structure , bioactivity and corrosion behaviour of B 2 O 3 – SiO 2 – Na 2 O – CaO glasses-investigation by spectroscopic methods 2018;84:292–300. https://doi.org/10.1016/j.optmat.2018.07.024.

[33] El-Tabey AE, Bedir AG, Khamis EA, Abd-El-Raouf M, Zahran F, Yousef MA, et al. Synthesis and evaluation of new poly cationic surfactants as corrosion inhibitors for carbon steel in formation water. Egypt J Chem 2020;63:833–50. https://doi.org/10.21608/ejchem.2019.11344.1730.

[34] Aiad I, El-Sukkary MM, El-Deeb A, El-Awady MY, Shaban SM. Surface and biological activity of some prepared iminium surfactants based on Schiff bases. J Surfactants Deterg 2013;16:243–50. https://doi.org/10.1007/s11743-012-1402-8.

[35] Elaraby A, Faisal K, Mohamed SK, El-sharkawy EA. Multi-scale quantum (DFT , MCs and MDs) insights and electrochemical validation of di-imine Schiff base inhibitor for carbon steel corrosion control in 1 M HCl solution. Appl Mater Today 2025;42:102615. https://doi.org/10.1016/j.apmt.2025.102615.

[36] Mahmoud SB, Elaraby A, Abd-El-Raouf M, Zaki EG. Hydrogen Production and Electrochemical Investigations of an Environmentally Salicornia Extract as a Green Corrosion Inhibitor in a 1 M HCl Solution. Egypt J Chem 2024. https://doi.org/10.21608/ejchem.2024.316943.10308.

[37] Basiony NM El, Nasser A, Hafez E, Elaraby A, Shafek SH, Elged AH, et al. Retard the corrosion reaction of carbon steel in acid solutions using Gemini-nonionic surfactant : Theoretical and experimental studies. Mater Today Commun 2023;37:107378. https://doi.org/10.1016/j.mtcomm.2023.107378.

[38] Salim M, Azab MM, Abo-Riya MA, Abd-El-Raouf M, EL Basiony NM. Controlling C-steel dissolution in 1 M HCl solution using newly synthesized ρ-substituted imine derivatives: Theoretical (DFT and MCs) and experimental investigations. J Mol Struct 2023;1274:134357. https://doi.org/10.1016/j.molstruc.2022.134357.

[39] Shaban SM, Elbhrawy MF, Fouda AS, Rashwan SM, Ibrahim HE, Elsharif AM. Corrosion inhibition and surface examination of carbon steel 1018 via N-(2-(2-hydroxyethoxy)ethyl)-N,N-dimethyloctan-1-aminium bromide in 1.0 M HCl. J Mol Struct 2021;1227:129713. https://doi.org/10.1016/j.molstruc.2020.129713.

[40] Luo W, Lin Q, Ran X, Li W, Tan B, Fu A, et al. A new pyridazine derivative synthesized as an efficient corrosion inhibitor for copper in sulfuric acid medium: Experimental and theoretical calculation studies. J Mol Liq 2021;341:117370. https://doi.org/10.1016/j.molliq.2021.117370.

[41] Elaraby A, Elgendy A, Migahed MA, Abdullah AM, Alharbi SM, Shaban SM, et al. Synthesis of Gemini cationic surfactants based on natural nicotinic acid and evaluation of their inhibition performance at C-steel/1M HCl interface_ Electrochemical and computational investigations. Colloids Surfaces A Physicochem Eng Asp 2022:130687. https://doi.org/10.1016/j.colsurfa.2022.130687.

[42] Haldhar R, Jayprakash Raorane C, Mishra VK, Periyasamy T, Berisha A, Kim SC. Development of different chain lengths ionic liquids as green corrosion inhibitors for oil and gas industries: Experimental and theoretical investigations. J Mol Liq 2023;372:121168. https://doi.org/10.1016/j.molliq.2022.121168.

[43] Lesar A, Milošev I. Density functional study of the corrosion inhibition properties of 1,2,4-triazole and its amino derivatives. Chem Phys Lett 2009;483:198–203. https://doi.org/10.1016/j.cplett.2009.10.082.

[44] El-Tabei AS, El-Azabawy OE, El Basiony NM, Hegazy MA. Newly synthesized quaternary ammonium bis-cationic surfactant utilized for mitigation of carbon steel acidic corrosion; theoretical and experimental investigations. J Mol Struct 2022;1262:133063. https://doi.org/10.1016/j.molstruc.2022.133063.

[45] Hegazy MA. Novel cationic surfactant based on triazole as a corrosion inhibitor for carbon steel in phosphoric acid produced by dihydrate wet process. J Mol Liq 2015;208:227–36. https://doi.org/10.1016/j.molliq.2015.04.042.

[46] Uhlig HH, King C V. Corrosion and Corrosion Control. J Electrochem Soc 1972;119:327C.

https://doi.org/10.1149/1.2404108.

[47] Zhang QH, Li YY, Lei Y, Wang X, Liu HF, Zhang GA. Comparison of the synergistic inhibition mechanism of two eco-friendly amino acids combined corrosion inhibitors for carbon steel pipelines in oil and gas production. Appl Surf Sci 2022;583. https://doi.org/10.1016/j.apsusc.2022.152559.

[48] Ragheb DM, Abdel-Gaber AM, Mahgoub FM, Mohamed ME. Eco-friendly method for construction of superhydrophobic graphene-based coating on copper substrate and its corrosion resistance performance. Sci Rep 2022;12:1–14. https://doi.org/10.1038/s41598-022-22915-5.

[49] Wang DY, Wang JH, Li HJ, Wu YC. Pectin-amino acid derivatives as highly efficient green inhibitors for the corrosion of N80 steel in CO2-saturated formation water. Ind Crops Prod 2022;189:115866. https://doi.org/10.1016/j.indcrop.2022.115866.

[50] Mobin M, Aslam R, Salim R, Kaya S. An investigation on the synthesis, characterization and anti-corrosion properties of choline based ionic liquids as novel and environmentally friendly inhibitors for mild steel corrosion in 5% HCl. J Colloid Interface Sci 2022;620:293–312. https://doi.org/10.1016/j.jcis.2022.04.036.

[51] El-Tabei AS, El-Azabawy OE, Basiony NM El, Hegazy MA. Newly synthesized quaternary ammonium bis-cationic surfactant utilized for mitigation of carbon steel acidic corrosion; theoretical and experimental investigations. J Mol Struct 2022;1262:133063. https://doi.org/10.1016/j.molstruc.2022.133063.

[52] Gholivand K, Sarmadi-Babaee L, Faraghi M, Badalkhani-Khamseh F, Fallah N. Heteroatom-containing phosphoramides as carbon steel corrosion inhibitors: Density functional theory and molecular dynamics simulations. Chem Phys Impact 2022;5:100099. https://doi.org/10.1016/j.chphi.2022.100099.

[53] Jabbar AH, Kamona SMH, Abbood SK, Hussein TK, Al-Saidi DN, Hameed SM, et al. The effective and sustainable application of a green amino acid-based corrosion Inhibitor for Cu metal. Chem Phys Impact 2023;7:100316. https://doi.org/10.1016/j.chphi.2023.100316.

[54] Solmaz R, Kardaş G, Çulha M, Yazici B, Erbil M. Investigation of adsorption and inhibitive effect of 2-mercaptothiazoline on corrosion of mild steel in hydrochloric acid media. Electrochim Acta 2008;53:5941–52. https://doi.org/10.1016/j.electacta.2008.03.055.

[55] Mobin M, Aslam R. Experimental and theoretical study on corrosion inhibition performance of environmentally benign non-ionic surfactants for mild steel in 3.5% NaCl solution. Process Saf Environ Prot 2018;114:279–95. https://doi.org/10.1016/j.psep.2018.01.001.

[56] El-tabey AE, Elaraby A, Elsharaky EA. Inhibition performance of gemini cationic surfactants for carbon steel in formation water: Electrochemical and computational investigations. J Mol Liq 2024:125452. https://doi.org/10.1016/j.molliq.2024.125452.

[57] Elaraby A, Elgendy A, Abd-El-Raouf M, Migahed MA, El-Tabei AS, Abdullah AM, et al. Synthesis of Gemini cationic surfactants based on natural nicotinic acid and evaluation of their inhibition performance at C-steel/1 M HCl interface: Electrochemical and computational investigations. Colloids Surfaces A Physicochem Eng Asp 2023;659:130687. https://doi.org/10.1016/j.colsurfa.2022.130687.

[58] Elaraby A, Abd S, Eman A, Zaki EG. Theoretical and electrochemical evaluation of tetra - cationic surfactant as corrosion inhibitor for carbon steel in 1 M HCl. Sci Rep 2023:1–18. https://doi.org/10.1038/s41598-023-27513-7.

[59] Li X, Chen L, Xie B, Lai C, He J, Feng J, et al. Two semi flexible nonplanar double Schiff bases as corrosion inhibitors for mild steel in HCl solution: Experimental and theoretical investigations. J Environ Chem Eng 2023;11:110077. https://doi.org/10.1016/j.jece.2023.110077.

[60] Guo L, Tan J, Kaya S, Leng S, Li Q, Zhang F. Multidimensional insights into the corrosion inhibition of 3,3-dithiodipropionic acid on Q235 steel in H2SO4 medium: A combined experimental and in silico investigation. J Colloid Interface Sci 2020;570:116–24. https://doi.org/10.1016/j.jcis.2020.03.001.

[61] El Guesmi N, Asghar BH, Awad MI, Al Harbi AN, Kassem MA, Shaaban MR. Novel thiazole-derived Schiff-Bases as efficient corrosion inhibitors for mild steel in acidic Media: Synthesis, electrochemical and Computational insights. Arab J Chem 2024;17:105867. https://doi.org/10.1016/j.arabjc.2024.105867.

[62] Huang L, Li HJ, Wu YC. Comprehensive evaluation of corrosion inhibition performance and ecotoxicological effect of cinchona IIa as a green corrosion inhibitor for pickling of Q235 steel. J Environ Manage 2023;335:117531. https://doi.org/10.1016/j.jenvman.2023.117531.

[63] Gao Y, Zhang J, Wang D, Fan J, Mol A, Wang F, et al. Naturally effective inhibition of microbial corrosion on carbon steel by beneficial biofilm in the South China Sea. Colloid Interface Sci Commun 2024;59:100779. https://doi.org/10.1016/j.colcom.2024.100779.

[64] Fouad SS, Parditka B, Nabil M, Baradács E, Negm S, Erdélyi Z. Effect of Cu interlayer on opto-electrical parameters of ZnO thin films. J Mater Sci Mater Electron 2022;33:20594–603. https://doi.org/10.1007/s10854-022-08871-w.

[65] Fouad SS, Sakr GB, Yahia IS, Basset DMA. Structural characterization and novel optical properties of defect chalcopyrite ZnGa2Te4 thin films. Mater Res Bull 2011;46:2141–6. https://doi.org/10.1016/j.materresbull.2011.06.002.

[66] El-Bana MS, El Radaf IM, Fouad SS, Sakr GB. Structural and optoelectrical properties of nanostructured LiNiO2thin films grown by spray pyrolysis technique. J Alloys Compd 2017;705:333–9. https://doi.org/10.1016/j.jallcom.2017.02.106.

[67] Sharma N, Sharma S, Sharma R. Dielectric and optical studies of CdSe nanoparticles : green synthesis. J Mater Sci Mater Electron 2020;31:16592–9. https://doi.org/10.1007/s10854-020-04214-9.

[68] Ahmad F, Maqsood A. Structural, dielectric, impedance, complex modulus, and optical study of Ni-doped Zn(1−x)NixO nanostructures at high temperatures. Mater Res Express 2021;8. https://doi.org/10.1088/2053-1591/ac2fcd.

[69] Lifshitz E. Optical properties of CdSe nanoparticle films prepared by chemical deposition and sol – gel methods 1998:188–96.
[70] Rao DR, Hariharan K, Vijayalakshmi KR. Synthesis of L [U 14C] α,β diaminopropionic acid. Indian J Biochem Biophys 1974;11:265–6.
[71] Yadav M, Gope L, Kumari N, Yadav P. Corrosion inhibition performance of pyranopyrazole derivatives for mild steel in HCl solution: Gravimetric, electrochemical and DFT studies. J Mol Liq 2016;216:78–86. https://doi.org/10.1016/j.molliq.2015.12.106.
[72] Liu H, Fan B, Fan G, Ma Y, Hao H, Zhang W. Anti-corrosive mechanism of poly (N-ethylaniline)/sodium silicate electrochemical composites for copper: Correlated experimental and in-silico studies. J Mater Sci Technol 2021;72:202–16. https://doi.org/10.1016/j.jmst.2020.08.064.
[73] Nnaji NJN, Ujam OT, Ibisi NE, Ani JU, Onuegbu TO, Olasunkanmi LO, et al. Morpholine and piperazine based carboxamide derivatives as corrosion inhibitors of mild steel in HCl medium. J Mol Liq 2017;230:652–61. https://doi.org/10.1016/j.molliq.2017.01.075.
[74] Badawi A, Alharthi SS, Alotaibi AA, Althobaiti MG. Investigation of the mechanical and electrical properties of SnS filled PVP/PVA polymeric composite blends. J Polym Res 2021;28. https://doi.org/10.1007/s10965-021-02569-z.
[75] Fouad SS, Baradács E, Nabil M, Parditka B, Negm S, Erdélyi Z. Microstructural and optical duality of TiO2/Cu/TiO2 trilayer films grown by atomic layer deposition and DC magnetron sputtering. Inorg Chem Commun 2022;145. https://doi.org/10.1016/j.inoche.2022.110017.
[76] Pal J, Chauhan P. Structural and optical characterization of tin dioxide nanoparticles prepared by a surfactant mediated method. Mater Charact 2009;60:1512–6. https://doi.org/10.1016/j.matchar.2009.08.007.
[77] Nabil M, Fouad SS, Easawi K, Abdallah S, Horia F. Novel correlations between optical absorption and water desalination of Ag / Fe 3 O 4 nanocomposite prepared by pulsed laser ablation in liquid. Opt Laser Technol 2023;164:109545. https://doi.org/10.1016/j.optlastec.2023.109545.
[78] Sudhakhar NSKS. Extensive studies on the electrochemical , photocatalytic and antimicrobial applications of bio assisted nano titania. SN Appl Sci 2023. https://doi.org/10.1007/s42452-023-05536-z.
[79] Zhao J, Liu L, Wang X, Gao W, Wang Z, Zhang X, et al. Materials Science & Engineering B The influence of anionic surfactant (SDS) on the optical , magnetic and capacitive properties of NiO nanocrystals via gas-liquid diffusion synthesis. Mater Sci Eng B 2024;299:116970. https://doi.org/10.1016/j.mseb.2023.116970.
[80] Nabil M, F H, Fouad SS, Negm S. Impact of Au nanoparticles on the thermophysicalparameters of Fe3O4 nanoparticles for seawater desalination. Opt Mater (Amst) 2022;128:112456. https://doi.org/10.1016/j.optmat.2022.112456.
[81] Fouad SS, Parditka B, Nabil M, Baradács E, Negm S, Atyia HE, et al. Bilayer number driven changes in polarizability and optical property in ZnO/TiO2 nanocomposite films prepared by ALD. Optik (Stuttg) 2021;233. https://doi.org/10.1016/j.ijleo.2021.166617.
[82] Salem JK, Hammad TM. The effect of surfactants on the particle size and optical properties of precipitated ZnO nanoparticles The effect of surfactants on the particle size and optical properties of precipitated ZnO nanoparticles 2014.
[83] Kushwaha P, Chauhan P. Influence of different surfactants on morphological , structural , optical , and magnetic properties of α - Fe 2 O 3 nanoparticles synthesized via co - precipitation method. Appl Phys A 2022;128:1–14. https://doi.org/10.1007/s00339-021-05157-6.
[84] El-Dougdoug WI, Al-Gorair AS, Abou Elsaoud A, Hawsawi H, Elaraby A, Mabrouk ES, et al. Synthesis and assessment of Gemini cationic surfactants as inhibitors for corrosion of carbon steel in hydrochloric acid. Green Chem Lett Rev 2022;15:796–812. https://doi.org/10.1080/17518253.2022.2135389.
[85] Elaraby A, Qasim KF, Mohamed SK, El-Sharkawy EA, Abdelhamed S. Di-imine Schiff base inhibitor for carbon steel corrosion in 1 M HCl: Electrochemical, surface and theoretical investigations. J Environ Chem Eng 2024;12:111861. https://doi.org/10.1016/j.jece.2023.111861.
[86] Qasim KF, Abdelhamed S, Elaraby A, Mousa MA. Polyaniline impact on graphitic C3N4's structural and physicochemical properties for high stability energy storage systems: Practical and theoretical studies. J Ind Eng Chem 2024. https://doi.org/10.1016/j.jiec.2024.05.011.
[87] El-Nagar RA, Elaraby A, Nessim MI, Ghanem A. Designed imidazolium-based ionic liquids to capture carbon dioxide from natural gas. J Mol Liq 2024;401:124708. https://doi.org/10.1016/j.molliq.2024.124708.
[88] Zamindar S, Mandal S, Murmu M, Banerjee P. Unveiling the future of steel corrosion inhibition: a revolutionary sustainable odyssey with a special emphasis on N+-containing ionic liquids through cutting-edge innovations. M Adv RSC, 2024;5 :4563. https://doi.org/10.1039/d4ma00156g.
[89] Bounedjar N, Ferhat M F, Toukal L , Messai R. Non thermal plasma synthesis of ZnO nanoparticles and their corrosion inhibition activity on XC70 mild steel pipeline in 1 M HCl acidic medium. Mater. Chem. Phys., 2024;311:128555. https://doi.org/10.1016/j.matchemphys.2023.128555
[90] Jeena T, Geetha M P, Suchetan P A, Ronald N, Amrutha K.Influence of cobalt doping on chemical and green synthesized magnesium oxide nanoparticles for enhanced photocatalytic evaluation, adsorption studies, antimicrobial analysis and corrosion inhibition study.In. Chem.Commu.2023;157. 111232, https://doi.org/10.1016/j.inoche.2023.111232